1900+14. I. An interpretive study of BeppoSAX and Ulysses observations. *Astrophys. J.* **549,** 1021–1038 (2001).
10. Gaensler, B. M. *et al.* Second-epoch VLA observations of SGR 1806−20. *GRB Circ. Network* **2933** (2005).
11. Corbel, S. & Eikenberry, S. S. The connection between W31, SGR 1806−20, and LBV 1806−20: Distance, extinction, and structure. *Astron. Astrophys.* **419,** 191–201 (2004).
12. Kolpak, M. A., Jackson, J. M., Bania, T. M. & Dickey, J. M. The radial distribution of cold atomic hydrogen in the galaxy. *Astrophys. J.* **578,** 868–876 (2002).
13. Corbel, S. *et al.* The distance of the soft gamma repeater SGR 1806−20. *Astrophys. J.* **478,** 624–630 (1997).
14. Hartmann, D. & Burton, W. B. *Atlas of Galactic Neutral Hydrogen*. Ch. 4, 169 (Cambridge Univ. Press, Cambridge, 1997).
15. Garwood, R. W. & Dickey, J. M. Cold atomic gas in the inner Galaxy. *Astrophys. J.* **338,** 841–861 (1989).
16. Figer, D. F., Najarro, F. & Kudritzki, R. P. The double-lined spectrum of LBV 1806−20. *Astrophys. J.* **610,** L109–L112 (2004).
17. Nakar, E., Gal-Yam, A., Piran, T., Fox, D. B. The distances of short-hard GRBs and the SGR connection. *Astrophys. J.* (submitted); preprint at http://arXiv.org/astro-ph/0502148 (2005).
18. Fuchs, Y. *et al.* ISO observations of the environment of the soft gamma-ray repeater SGR 1806−20. *Astron. Astrophys.* **350,** 891–899 (1999).
19. Gaensler, B. M. *et al.* A stellar wind bubble coincident with the anomalous X-ray pulsar 1E 1048.1-5937: Are magnetars formed from massive progenitors? *Astrophys. J.* **620,** L95–L98 (2005).
20. Pacholczyk, A. G. *Radio Astrophysics. Nonthermal Processes in Galactic and Extragalactic Sources* (Series of Books in Astronomy and Astrophysics, Freeman, San Francisco, 1970).
21. Scott, M. A. & Readhead, A. C. S. The low-frequency structure of powerful radio sources and limits to departures from equipartition. *Mon. Not. R. Astron. Soc.* **180,** 539–550 (1977).
22. Frail, D. A., Waxman, E. & Kulkarni, S. R. A 450-day light curve of the radio afterglow of GRB 970508: Fireball calorimetry. *Astrophys. J.* **537,** 191–204 (2000).
23. Cheng, K. S. & Wang, X. Y. The radio afterglow from the giant flare of SGR 1900+14: The same mechanisms as afterglows from classic gamma-ray bursts? *Astrophys. J.* **593,** L85–L88 (2003).
24. Nakar, E., Piran, T., Sari, R. Giant flares as mini gamma ray bursts. Preprint at http://arXiv.org/astro-ph/0502052 (2005).
25. Wang, X. Y., Wu, X. F., Fan, Y. Z., Dai, Z. G. & Zhang, B. An energetic blast wave from the December 27 giant flare of soft γ-ray repeater 1806−20. *Astrophys. J.* **623**, L29–L32 (2005).
26. Hjellming, R. M. *et al.* Light curves and radio structure of the 1999 September transient event in V4641 Sagittarii (= XTE J1819-254 = SAX J1819.3-2525). *Astrophys. J.* **544,** 977–992 (2000).

Supplementary Information accompanies the paper on **www.nature.com/nature**.

Acknowledgements ATCA is funded by the Commonwealth of Australia for operations as a National Facility managed by CSIRO. We thank K. Newton-McGee and B. Gaensler for scheduling and performing observations with the ATCA. GMRT is run by the National Centre for Radio Astrophysics—Tata Institute of Fundamental Research, India. We thank the GMRT staff and in particular C. H. Ishwara-Chandra and D. V. Lal for help with observations and analysis. The VLA is a facility of the National Science Foundation operated under cooperative agreement by Associated Universities, Inc. NMA is a branch of the National Astronomical Observatory, National Institutes of Natural Sciences, Japan. IRAM is supported by INSU/CNRS (France), MPG (Germany) and IGN (Spain). We thank A. Weiss from IRAM for help with the observations. We gratefully acknowledge discussions with S. Corbel, S. S. Eikenberry and R. Sari. Our work is supported in part by the NSF and NASA.

Competing interests statement The authors declare that they have no competing financial interests.

Correspondence and requests for materials should be addressed to P.B.C. (pbc@astro.caltech.edu).

Observation of nuclear fusion driven by a pyroelectric crystal

B. Naranjo[1], **J.K. Gimzewski**[2,3] **& S. Putterman**[1,3]

[1]*Physics Department,* [2]*Chemistry Department,* [3]*CNSI, University of California Los Angeles, California 90095, USA*

While progress in fusion research continues with magnetic[1] and inertial[2] confinement, alternative approaches—such as Coulomb explosions of deuterium clusters[3] and ultrafast laser–plasma interactions[4]—also provide insight into basic processes and technological applications. However, attempts to produce fusion in a room temperature solid-state setting, including 'cold' fusion[5] and 'bubble' fusion[6], have met with deep scepticism[7]. Here we report that gently heating a pyroelectric crystal in a deuterated atmosphere can generate fusion under desktop conditions. The electrostatic field of the crystal is used to generate and accelerate a deuteron beam (>100 keV and >4 nA), which, upon striking a deuterated target, produces a neutron flux over 400 times the background level. The presence of neutrons from the reaction D + D → ^{3}He (820 keV) + n (2.45 MeV) within the target is confirmed by pulse shape analysis and proton recoil spectroscopy. As further evidence for this fusion reaction, we use a novel time-of-flight technique to demonstrate the delayed coincidence between the outgoing α-particle and the neutron. Although the reported fusion is not useful in the power-producing sense, we anticipate that the system will find application as a simple palm-sized neutron generator.

Because its spontaneous polarization is a function of temperature, heating or cooling a pyroelectric crystal in vacuum causes bound charge to accumulate on faces normal to the polarization. A modest change in temperature can lead to a surprisingly large electrostatic field. For example, heating a lithium tantalate crystal from 240 K to 265 K decreases its spontaneous polarization by $0.0037\,C\,m^{-2}$ (ref. 8). In the absence of spurious discharges, introducing this magnitude of surface charge density into the particular geometry of our experiment (Fig. 1a, b) gives a potential of 100 kV. Attempts to harness this potential have focused on electron acceleration and the accompanying bremsstrahlung radiation[9–12], but using the crystal to produce and accelerate ions has been studied much less. Seeking to drive the D–D fusion reaction (http://www.physics.ucla.edu/~naranjo/ucei/ucei.pdf; http://neer.inel.gov/abstract.asp?ProjectID=126; http://www.binghamton.edu/physics/Brownridge%20Summary.pdf), we set out to develop a method of reliably producing an ion beam of sufficient energy (>80 keV) and current (>1 nA). We demonstrate such a method using a tungsten tip to generate the high field ($>25\,V\,nm^{-1}$) necessary for gas phase field ionization of deuterium.

A cut-away view of our vacuum chamber is shown in Fig. 1c. We mounted a cylindrical (diameter, 3.0 cm; height, 1.0 cm) z-cut $LiTaO_3$ crystal with negative axis facing outward onto a hollow copper block. On the exposed crystal face, we attached a copper disc (diameter, 2.5 cm; height, 0.5 mm), allowing charge to flow to a tungsten probe (shank diameter, 80 μm; tip radius, 100 nm; length, 2.3 mm) (Fig. 1b). The probe geometry was chosen so that the tip field was approximately $25\,V\,nm^{-1}$ when the crystal face was charged to 80 kV.

Our detector arrangement is shown in Fig. 1d. The neutron detector consists of six liquid scintillator (BC-501A and NE213) cells (diameter, 127 mm; height, 137 mm), each optically coupled to a 127-mm Hamamatsu R1250 photomultiplier tube (PMT). One output of each PMT was fed into a logical OR trigger, while the other output was fed into two Acqiris DC270 8-bit (1 gigasample per second) 4-channel digitizers configured as a single 8-channel digitizer. For every trigger, a 650-ns waveform was digitized simultaneously on all channels and written to disk for later analysis.

A typical run is shown in Fig. 2. The chamber's deuterium pressure was held at 0.7 Pa throughout the run. First, the crystal was cooled down to 240 K from room temperature by pouring liquid nitrogen into the cryogenic feedthrough. At time $t = 15$ s, the heater was turned on. At $t = 100$ s, X-ray hits due to free electrons striking the crystal were recorded. At $t = 150$ s, the crystal had reached 80 kV and field ionization was rapidly turning on. At $t = 160$ s and still not above 0 °C, the neutron signal rose above background. Ions striking the mesh and the surrounding aperture created secondary electrons that accelerated back into the crystal, increasing the X-ray signal. At $t = 170$ s, the exponential growth of the ion current had ceased, and the tip was operating in the strong field regime, in which neutral molecules approaching the tip ionize with unity probability. The neutron flux continued to increase along with crystal potential until $t = 220$ s, when we shut off the heater. Then, the crystal lost charge through field ionization faster than the

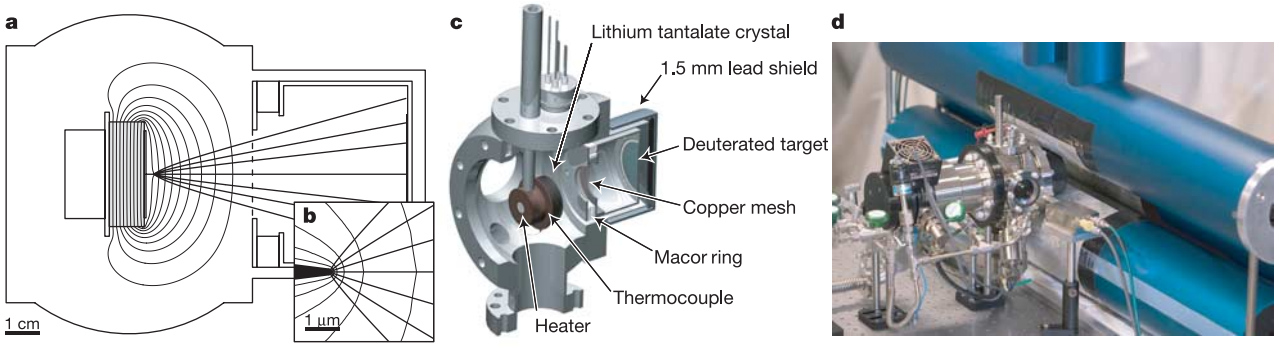

Figure 1 Experiment geometry. **a**, Calculated equipotentials and D^+ trajectories for a crystal charged to 100 kV; calculations were performed using finite-element methods. The grounded copper mesh (85% open area, 19.8-μm wire; vertical dashed line) shields the Faraday cup (right). The cup and target are connected to a Keithley 6485 picoammeter and biased to +40 V to collect secondary electrons and help prevent avalanche discharges. **b**, Same trajectories shown near the tip. Using a shorter tip reduces the beam's angular spread. **c**, Vacuum chamber cut-away view. D_2 pressure was set using a leak valve and monitored with a D_2 compensated Pirani gauge. The target was a molybdenum disc coated with ErD_2. **d**, Arrangement of neutron and X-ray detectors (Amptek XR-100T-CdTe). To better resolve the bremsstrahlung endpoint, a 2.5-cm aluminium filter (not shown) was placed between the X-ray detector and the viewport. The vacuum chamber's thick stainless steel walls and lead sheet shielded the neutron detector from X-rays.

reduced pyroelectric current could replace it, resulting in a steadily decreasing crystal potential. At $t = 393$ s, the crystal spontaneously discharged by sparking, halting the effect.

Pulse shape analysis and proton recoil spectroscopy of neutron detector data collected during the run are shown in Fig. 3. (See Supplementary Methods for details on neutron detector calibration, pulse shape analysis, and a Monte Carlo calculation of detector response and efficiency.) The majority of background triggers, as collected in the first 100 s of the run, have an electron recoil shape (900 counts per second) and are due to cosmic muons and γ-rays, compared with relatively few triggers having a proton recoil shape (33 counts in the first 100 s). Correcting for our 18% 2.45-MeV neutron detection efficiency, the observed peak neutron flux was 800 neutrons per second. We may compare this observed peak

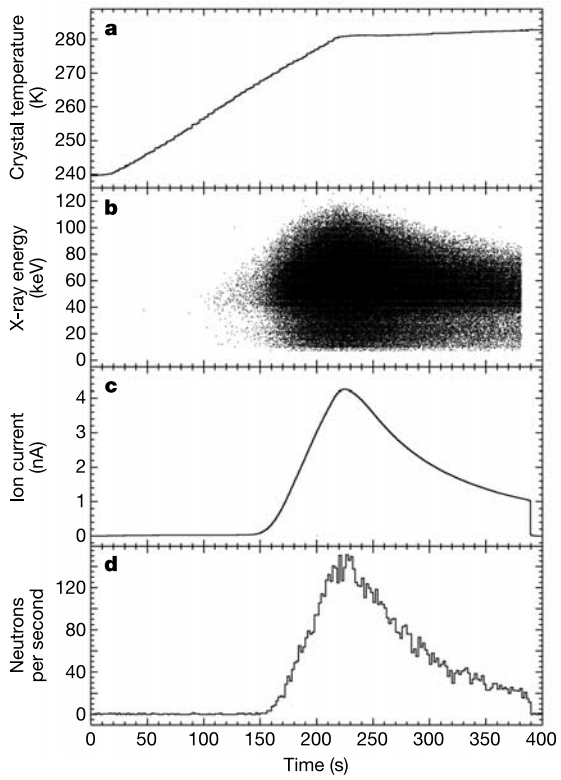

Figure 2 Data from a single run (see also Supplementary Movie 1). **a**, Crystal temperature. The heating rate was 12.4 K min^{-1}, corresponding to a pyroelectric current of 22 nA and a heating power of 2 W. **b**, X-rays detected. **c**, Faraday cup current. **d**, Neutrons detected.

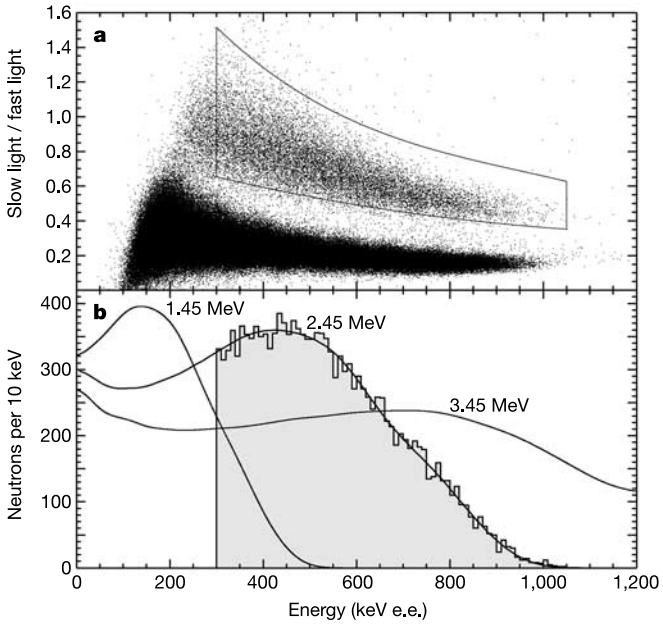

Figure 3 Neutron spectroscopy for the single run. The energy scale, given in electron equivalent (e.e.) energy, was calibrated against Compton edges of a series of γ-ray sources and is proportional to anode charge. **a**, Pulse shape discrimination (PSD) spectrum. Our PSD variable 'slow light/fast light' is the ratio of integrated light in the tail of the PMT signal generated by an event in the liquid scintillator, to the integrated light around the signal's peak. Electron recoils are in the lower branch, and proton recoils, having longer scintillation decay, are in the upper branch. The events enclosed within the upper region are compared against tabulated pulse shapes, rejecting unusual events such as PMT double pulsing. There were a total of 15,300 valid neutrons over the course of the 400-s run. From the distribution of events, we estimate that the number of electron events leaking into the proton branch is negligible compared to the 1% cosmic background. **b**, Proton recoil spectrum. Valid neutron events are shown in histogram format. For comparison, we also show our detector's simulated[20,21] responses to 1.45 MeV, 2.45 MeV and 3.45 MeV centre-of-mass boosted neutrons.

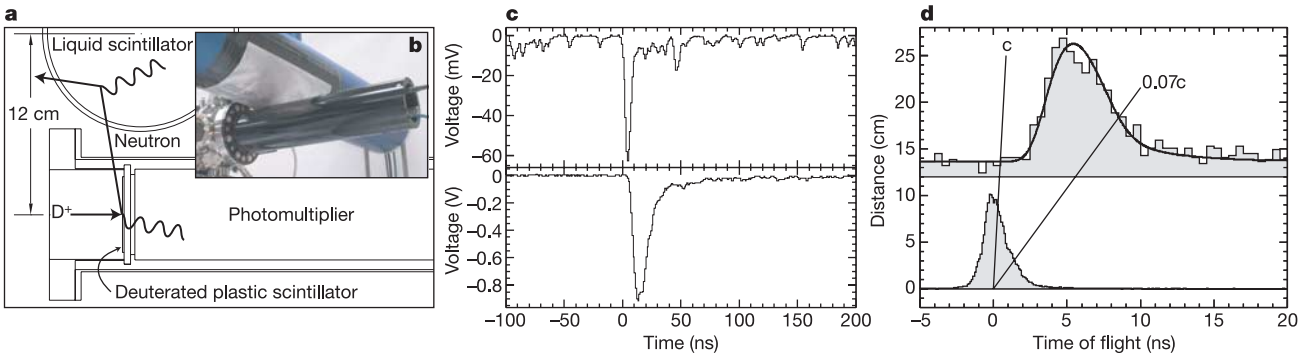

Figure 4 Neutron time-of-flight measurement. **a**, A deuteron is shown striking a thin disk of deuterated plastic scintillator, where it fuses with another deuteron, producing an 820-keV ^{3}He and a 2.45-MeV neutron. The α-particle promptly scintillates in the plastic, recorded by a photomultiplier tube coupled to the glass UHV viewport through a silicone optical pad. The neutron, on the other hand, leaves the vacuum chamber, and is shown detected via proton recoil in the liquid scintillator. **b**, Experiment geometry. **c**, Simultaneously captured PMT traces, demonstrating an α-particle–neutron coincidence. The plastic scintillator trace, shown in the upper panel, has a large α-particle hit at $t = 0$ ns, whereas the smaller hits are incident deuterons that stopped in the plastic but did not fuse. The liquid scintillator trace, shown in the lower panel, has a proton hit at $t = 6$ ns. **d**, Time-of-flight results. The distribution of neutron flight times is shown in the upper histogram. As the neutron emission and detection volumes are finite and relatively closely spaced, we observe a range of flight times. The Monte Carlo flight time distribution, including a constant term to account for background, is shown fitted. The peak in the distribution roughly corresponds with the 5.6 ns it takes a 2.45-MeV neutron moving with a velocity of $0.07c$ (where c is the speed of light) to travel 12 cm. The relative timing offset between the two PMTs was calibrated using back-to-back 511-keV γ-rays from a ^{22}Na source, as shown in the lower histogram.

neutron flux to the neutron flux expected from the ion beam striking the ErD_2 target. At the time of peak neutron flux, the ion current was 4.2 nA and the accelerating potential, inferred from the bremsstrahlung endpoint, was 115 kV. Using tabulated stopping powers[13] and fusion cross-sections[14], we calculate a neutron flux of 900 neutrons s^{-1}. This is a slight overestimate, because part of the ion beam struck outside the target and there was an oxide layer on the target.

In Fig. 4, we present our neutron time-of-flight measurement. Using deuterated plastic scintillator (BC-436) as both a deuterated target, and as a scintillation material, allowed us to pinpoint individual fusion events. The scintillator was mounted inside the chamber against a glass ultrahigh-vacuum (UHV) viewport, through which a Hamamatsu H1949-50 PMT was coupled via a silicone optical pad. The side of the scintillator facing the beam had a 50-nm layer of evaporated aluminium and was connected to the picoammeter. The aluminium prevented the target from charging up, allowed for a reliable beam current measurement, and helped screen out stray light originating from within the chamber. To minimize background hits, yet still collect valid coincidences, we used a reduced deuterium pressure and a reduced heating rate so that the ion current was around 10 pA. Running at this low level permitted prolonged runs. For example, the data shown in Fig. 4d were taken from a single heating cycle lasting over eight hours.

We have shown that small (about centimetre-sized) pyroelectric crystals can produce ion beams (see also Supplementary Fig. 1 and Supplementary Movie 2) of sufficient energy and current to drive nuclear fusion. We anticipate increasing the field ionization current by using a larger tip, or tip array, and by operating at cryogenic temperatures. With these enhancements, and in addition using a tritiated target, we believe that the reported signal could be scaled beyond 10^6 neutrons s^{-1}. Pyroelectric crystals may also have applications in electrostatic fusion devices[15], such as the Farnsworth fusor[16–18], and as microthrusters in miniature spacecraft[19]. □

Received 14 December 2004; accepted 30 March 2005; doi:10.1038/nature03575.

1. Shimomura, Y. & Spears, W. Review of the ITER project. *IEEE Trans. Appl. Supercond.* **14,** 1369–1375 (2004).
2. Miller, G. H., Moses, E. I. & Wuest, C. R. The National Ignition Facility: enabling fusion ignition for the 21st century. *Nucl. Fusion* **44,** S228–S238 (2004).
3. Ditmire, T. *et al.* Nuclear fusion from explosions of femtosecond laser-heated deuterium clusters. *Nature* **398,** 489–492 (1999).
4. Pretzler, G. *et al.* Neutron production by 200 mJ ultrashort laser pulses. *Phys. Rev. E* **58,** 1165–1168 (1998).
5. Taubes, G. *Bad Science: The Short Life and Weird Times of Cold Fusion* (Random House, New York, 1993).
6. Taleyarkhan, R. P. *et al.* Evidence for nuclear emissions during acoustic cavitations. *Science* **295,** 1868–1873 (2002).
7. Saltmarsh, M. J. & Shapira, D. Questions regarding nuclear emissions in cavitation experiments. *Science* **297,** 1603 (2002).
8. Glass, A. M. Dielectric, thermal, and pyroelectric properties of ferroelectric $LiTaO_3$. *Phys. Rev.* **172,** 564–571 (1968).
9. Rosenblum, B., Braunlich, P. & Carrico, J. P. Thermally stimulated field emission from pyroelectric $LiNbO_3$. *Appl. Phys. Lett.* **25,** 17–19 (1974).
10. Riege, H. Electron emission from ferroelectrics—a review. *Nucl. Instrum. Methods A* **340,** 80–89 (1994).
11. Brownridge, J. D., Shafroth, S. M., Trott, D. W., Stoner, B. R. & Hooke, W. M. Observation of multiple nearly monoenergetic electron production by heated pyroelectric crystals in ambient gas. *Appl. Phys. Lett.* **78,** 1158–1159 (2001).
12. Rosenman, G., Shur, D., Krasik, Ya. E. & Dunaevsky, A. Electron emission from ferroelectrics. *J. Appl. Phys.* **88,** 6109–6161 (2000).
13. Ziegler, J. F. The stopping of energetic ions in solids. *Nucl. Instrum. Methods* **168,** 17–24 (1980).
14. Bosch, H. S. & Hale, G. M. Improved formulas for fusion cross-sections and thermal reactivities. *Nucl. Fusion* **32,** 611–631 (1992).
15. Nevins, W. M. Can inertial electrostatic confinement work beyond the ion-ion collisional time scale? *Phys. Plasmas* **2,** 3804–3819 (1995).
16. Farnsworth, P. T. Electric discharge device for producing interactions between nuclei. US Patent No. 3258402 (1966).
17. Farnsworth, P. T. Method and apparatus for producing nuclear-fusion reactions. US Patent No. 3386883 (1968).
18. Hirsch, R. L. Inertial-electrostatic confinement of ionized fusion gases. *J. Appl. Phys.* **38,** 4522–4534 (1967).
19. Mitterauer, J. Micropropulsion for small spacecraft: a new challenge for field effect electric propulsion and microstructured liquid metal ion sources. *Surf. Interface Anal.* **36,** 380–386 (2004).
20. Agostinelli, S. *et al.* GEANT4 — a simulation toolkit. *Nucl. Instrum. Methods A* **506,** 250–303 (2003).
21. Verbinski, V. V. *et al.* Calibration of an organic scintillator for neutron spectrometry. *Nucl. Instrum. Methods* **65,** 8–25 (1968).

Supplementary Information accompanies the paper on **www.nature.com/nature**.

Acknowledgements The neutron detector was built with funds from DARPA. Funding for various stages of this project was provided by the NSF, ONR and DARPA. We thank W. Wright and K. O'Doherty for demonstrations of electron and ion emission from pyroelectrics, respectively; H. Lockart for machine workshop expertise; K. O'Doherty for evaporating the 50-nm film onto the plastic scintillator; R. Cousins for recommending the use of liquid scintillator for detection and pulse-shape identification of neutrons, and for overseeing the design and construction of a prototype detector using waveform digitization; and T. Venhaus, W. Harbin and J. Hoffer of LANL (ESA-TSE group) for supplying the deuterated target. S. P. thanks A. Erbil for bringing the phenomenon of ferroelectric emission to his attention, along with ref. 10.

Competing interests statement The authors declare that they have no competing financial interests.

Correspondence and requests for materials should be addressed to B.N. (naranjo@physics.ucla.edu).